A Nonlinear Stiffness Safe Joint Mechanism Design for Human Robot Interaction

Jung-Jun Park
e-mail: hantiboy@korea.ac.kr

Jae-Bok Song[1]
Mem. ASME
e-mail: jbsong@korea.ac.kr

School of Mechanical Engineering,
Korea University,
Anam-dong,
Seongbuk-gu,
Seoul 136-713, Korea

Service robots used in human environments must be designed to avoid collisions with humans. A safe robot arm can be designed using active or passive compliance methods. A passive compliance system composed of purely mechanical elements often provides faster and more reliable responses for dynamic collision than an active one involving sensors and actuators. Because positioning accuracy and collision safety are equally important, a robot arm should have very low stiffness when subjected to a collision force that could cause human injury but should otherwise maintain very high stiffness. A novel safe joint mechanism (SJM) consisting of linear springs and a double-slider mechanism is proposed to address these requirements. The SJM has variable stiffness that can be achieved with only passive mechanical elements. Analyses and experiments on static and dynamic collisions show high stiffness against an external torque less than a predetermined threshold value and an abrupt drop in stiffness when the external torque exceeds this threshold. The SJM enables the robotic manipulator to guarantee positioning accuracy and collision safety and it is simple to install between an actuator and a robot link without a significant change in the robot's design. [DOI: 10.1115/1.4001666]

Keywords: nonlinear stiffness, passive compliance, physical human-robot interaction, safety mechanism

1 Introduction

In recent years, service robots have received considerable attention. Because these robots work in human environments, safety issues related to physical human-robot interaction have become increasingly important. Therefore, several types of safety strategies have been proposed for collision safety between a human and a robot. First, when collision is predicted from noncontact sensors, the robot can avoid collision by generating a collision-free path in real time. Second, if collision is detected by contact sensors, the robot reacts to this collision by stopping itself or by generating a reflexive motion so as to minimize the collision force delivered to humans [1,2]. Third, when a relatively large collision occurs inevitably, the collision force can be absorbed by several passive compliance mechanisms.

A safe robot arm can be achieved by either an active or a passive compliance system. The first and second approaches in the previous paragraph are grouped into the active compliance system and the third approach falls into the passive compliance system. An actively compliant arm suffers from relatively low bandwidth unless sophisticated and expensive sensors and controllers are adopted to respond to dynamic collision. Furthermore, accurate dynamic parameters of a robot arm are required for fast detection and appropriate reaction, and possible sensor noise, and actuator malfunction should be considered.

In contrast, a robot arm based on passive compliance is usually composed of entirely mechanical elements such as a spring [3], a flexible link, and an artificial pneumatic muscle [4], which can absorb excessive collision force. Since this approach does not use any sensor or actuator for shock absorption, it can provide fast and reliable responses even for dynamic collision. To exploit this feature of passive compliance approach, variable stiffness joint mechanisms that can simultaneously control position and stiffness were proposed. They can be grouped into two categories. The first group is an antagonistic mechanism inspired by the musculoskeletal system [5,6]. A pair of actuators connected to the same joint through nonlinear springs exerts torque antagonistically to control both position and stiffness. The second group is a serial actuation composed of a motor for position control and a variable stiffness mechanism, which is connected to the position frame in series [7–9]. These variable stiffness joint mechanisms are advantageous to dexterous manipulation and their compliant motion is good for collision safety. However, extra actuators such as motors, electric dampers, or brakes for simultaneous control of position and stiffness cause an increase in the system size and weight of a robot arm, which may be dangerous from a point of view of collision safety. Furthermore, collision safety cannot be guaranteed while the variable stiffness mechanisms maintain high stiffness to conduct given tasks because it is usually difficult to quickly reduce their stiffness to a very low value.

Although a spring is by far the most popular mechanical element for shock absorption, a soft spring used at the joint of a robot arm leads to positioning inaccuracy due to its continuous operation even for small external forces, which do not require any actions for collision safety. This inaccuracy is often deteriorated by undesirable oscillations caused by the elastic behavior of a spring. On the other hand, a stiff spring can provide high positioning accuracy of a robot arm but it gives a higher probability of injury upon collision with humans because of its low capability of shock absorption.

An ideal safe manipulator would exhibit very low stiffness when subjected to a collision force greater than that which might cause human injury but would maintain very high stiffness otherwise. Of course, this ideal feature can be achieved by the active compliance approach but this approach often causes several shortcomings as previously mentioned. In our previous study, this ideal feature was realized using a safe link mechanism (SLM) and a safe joint mechanism (SJM) based on passive compliance [10–12]. The SLM installed at the middle of the link part of a robot arm can absorb a collision force in all directions except the

[1]Corresponding author.

Contributed by the Mechanisms and Robotics Committee of ASME for publication in the JOURNAL OF MECHANICAL DESIGN. Manuscript received July 22, 2009; final manuscript received April 8, 2010; published online May 25, 2010. Assoc. Editor: Ashitava Ghosal.

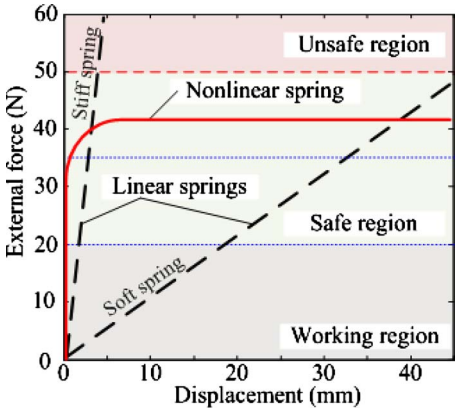

Fig. 1 Comparison between linear and nonlinear springs

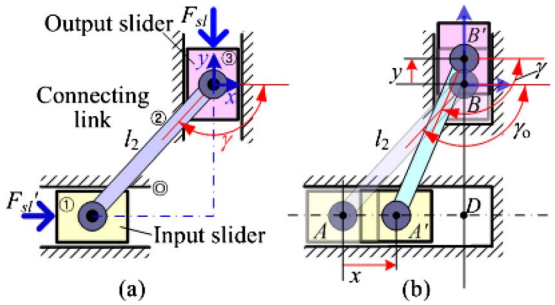

Fig. 2 (*a*) Double-slider mechanism and (*b*) zero configuration and general configuration

direction along the axis of SLM. However, the wire structure to transmit an external force to the nonlinear spring mechanism of the SLM often suffers from maintenance problems. On the other hand, the SJM installed at the joint part of a robot arm absorbs collision shock in the rotational direction. The first version of the safe joint mechanism (SJM-I) was developed for connection to the output shaft of the gear reducer such as a planetary gear reducer. The second version of the safe joint mechanism (SJM-II) was proposed to directly mount it at the output part of a harmonic drive, which led to a higher force transmission efficiency and more compact design than the SJM-I.

The SJM-II is mainly composed of linear springs and a double-slider mechanism. Springs are used to absorb collision force for safety while the double-slider mechanism determines the level of external force above which the SJM-II is activated. The main contribution of this proposed mechanism is the realization of the ideal nonlinear spring using only passive mechanical elements. Without compromising positioning accuracy for collision safety, both features can be achieved simultaneously with SJM-II. This paper presents the descriptive mathematical model of its nonlinear spring system to investigate how this mechanism works and responds to collision shock. Various kinematic and dynamic analyses were conducted using the exact model of the SJM-II to investigate the motion of the SJM-II and the robot arm equipped with it.

The rest of the paper is organized as follows. The analysis of the SJM-II is discussed in detail in Sec. 2. Section 3 presents further explanation about the analysis of the robot arm with the SJM-II. Various experimental results for both static and dynamic collisions are provided in Sec. 4. Finally, Sec. 5 presents conclusions and future work.

2 Principle of Operation of Safe Joint Mechanism

As previously mentioned, springs have been widely used in various safety mechanisms because of good shock-absorbing properties. However, a linear spring cannot be used directly in a robot arm because its displacement is proportional to the external force. A robot arm equipped with soft springs exhibits deflection due to its own weight and/or a small load, as shown in Fig. 1. This characteristic is advantageous to collision safety but leads to low positioning accuracy. To cope with this problem, we need a spring whose stiffness remains very high when the external force acting on the end-effector of the robot arm is within the range of normal operation but drops rapidly when the force exceeds a certain level due to collision with an object. However, no spring with this ideal feature exists. In this research, the nonlinear power transmission characteristics of a double-slider mechanism are exploited to achieve this nonlinear spring feature.

2.1 Static Analysis of Nonlinear Spring System. Consider the double-slider mechanism shown in Fig. 2. When a slider force F_{sl} is exerted on the output slider (link 3) in the y-axis direction, an appropriate force F'_{sl} acting on the slider (link 1) can maintain the static equilibrium of this mechanism. In the double-slider mechanism, the transmission angle γ is defined as the angle between the connecting link (link 2) and the line perpendicular to the output slider movement.

By applying the principle of virtual work, the relationship between F_{sl} and F'_{sl} is obtained by

$$F'_{sl}\delta x = F_{sl} \cdot \delta y \tag{1}$$

where δx and δy are the virtual displacements associated with the input slider motion and the output slider motion, respectively. Dividing Eq. (1) by the time interval yields

$$F'_{sl} = \frac{\dot{y}}{\dot{x}} F_{sl} \tag{2}$$

where $\dot{x}$ and $\dot{y}$ are the velocities of the input slider and the output slider, respectively. From the equation of closure of this mechanism shown in Fig. 2(b),

$$x = A\bar{D} - A'\bar{D} = -l_2 \cos\gamma_o + l_2 \cos\gamma \tag{3a}$$

$$y = B'\bar{D} - B\bar{D} = l_2 \sin\gamma_o - l_2 \sin\gamma \tag{3b}$$

where γ_o represents the transmission angle at the zero configuration. At the zero configuration, it is assumed that the output slider is blocked by the fixed link so that it cannot move farther down from this home position, as shown in Fig. 2(b). Differentiation of Eqs. (3a) and (3b) yields

$$\dot{x} = -\dot{y}\tan\gamma \tag{4}$$

Substituting Eq. (4) into Eq. (2), the force ratio of F'_{sl} to F_{sl} is given by

$$\frac{F'_{sl}}{F_{sl}} = -\cot\gamma \tag{5}$$

The force ratio varies nonlinearly depending on the transmission angle, as shown in Fig. 3. The larger γ is, the larger the value of F'_{sl} must be to maintain equilibrium for a given F_{sl}. As γ approaches 120 deg, a smaller value of F'_{sl} is required for equilibrium, thereby resulting in relatively easy movement of the output slider for a given F_{sl}.

To achieve the nonlinear spring characteristic shown in Fig. 1, a precompressed spring is installed between the output slider and the fixed link (link 0), as shown in Fig. 4. The spring force F_s can generate the slider force F_{sl}, as shown in Fig. 2(a). Consider another roller-link in which the roller of the input slider moves along the slot of the input link (link 4). To maintain static equilibrium of

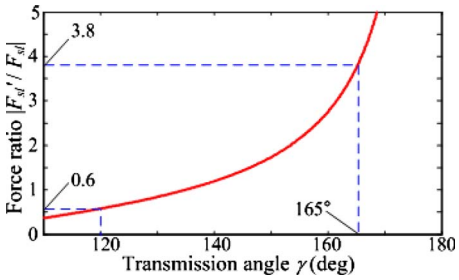

Fig. 3 Force ratio as a function of transmission angle

this mechanism, spring torque T_s exerted on O_1 induces force F_s'. By applying the principle of virtual work, the relationship between T_s and F_s is obtained by

$$T_s = \frac{\dot{y}}{\dot{\theta}_4} F_s \tag{6}$$

From the equation of closure of this mechanism shown in Fig. 4(*b*), we obtain

$$d\cos\theta_4 = l_2(\cos\gamma - \cos\gamma_o) \tag{7a}$$

$$d_o = -d\sin\theta_4 \tag{7b}$$

Substituting the differentiation of Eq. (7) into Eq. (6) yields

$$T_s = \frac{\dot{y}}{\dot{\theta}_4} F_s = \frac{d}{\tan\gamma\sin\theta_4} F_s \tag{8}$$

Consider a situation in which the input torque T_{in} is forced to act on the input link (link 4 in Fig. 4). Since the spring force caused by spring compression exists, the output slider cannot move upside until the input torque exceeds a certain threshold, which is large enough to move it upside. This input torque, required to initiate the movement of the output slider, is defined in this research as the threshold torque T_{th}. Once the input torque exceeds this threshold, the spring is rapidly compressed until the output slider moves to the uppermost position, where the spring can no longer be compressed. From Eq. (8), T_{th} can be described by

$$T_{th} = \frac{d_o}{\tan\gamma_o\sin\theta_{4o}} k s_o \tag{9}$$

where subscript o represents the zero configuration, s_o is the spring compression, d_o is the displacement between points A and O_1, γ_o is the transmission angle, θ_{4o} is the angular displacement of the input link, and k is the spring constant.

In Fig. 4(*b*), the spring torque required for equilibrium can be obtained from Eq. (8) as follows:

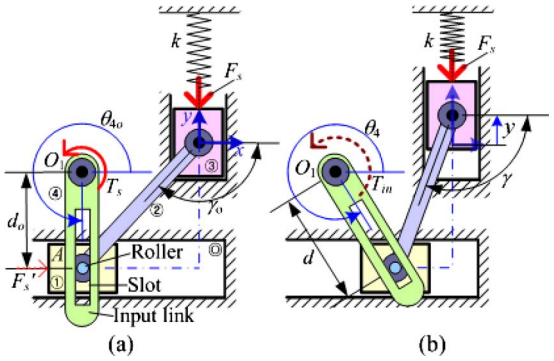

Fig. 4 Nonlinear spring system composed of a double-slider mechanism with a spring: (*a*) zero configuration and (*b*) general configuration

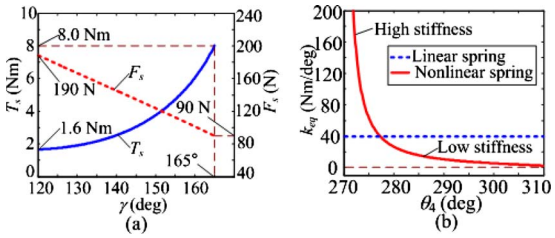

Fig. 5 (*a*) Spring torque and force versus transmission angle and (*b*) equivalent stiffness of nonlinear spring system as a function of angular displacement

$$T_s = k_{eq}(\theta_4 - \theta_{4o}) = \frac{d}{\tan\gamma\sin\theta_4} k(s_o + y) \tag{10}$$

where k_{eq} is the equivalent stiffness seen from the input link and x is the displacement of the output slider. Substituting Eqs. (3*a*) and (7*b*) into Eq. (10) yields the equivalent stiffness k_{eq} as a function of θ_4 as follows:

$$k_{eq} = \frac{d}{(\theta_4 - \theta_{4o})\tan\gamma\sin\theta_4} k(s_o + y) \tag{11}$$

For example, when k=5.6 kN/m, s_0=16 mm, l_2=26 mm, θ_{4o} =270 deg, and γ_o=165 deg, the threshold torque T_{th}=8.0 N m. From Eqs. (10) and (11), the spring torque T_s and the equivalent stiffness k_{eq} of this mechanism are plotted in Fig. 5 as functions of γ and θ_4, respectively. As the transmission angle decreases, F_s acting on the output slider increases because the spring is further compressed. However, T_s for the equilibrium of this mechanism decreases, on the contrary, since the transmission angle of the double-slider mechanism decreases continuously, as shown in Fig. 5(*a*). The equivalent stiffness k_{eq} is kept very high for initial value of θ_{4o}(=270 deg) but it quickly drops as θ_4 increases, as shown in Fig. 5(*b*). Hence, this nonlinear stiffness can be realized by the double-slider mechanism with a spring.

2.2 Dynamic Analysis of Nonlinear Spring System. In this section, dynamic equations of motion for the proposed nonlinear spring system are derived. Figure 6 shows the nonlinear spring

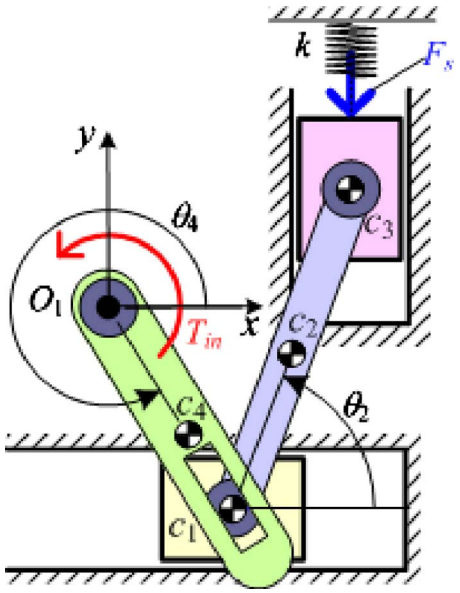

Fig. 6 Approximate dynamic analysis of nonlinear spring system

system and its related parameters. The Lagrangian formulation is used to develop the equations of motion.

For a general mechanical system consisting of n rigid bodies, Lagrange's equation can be written as

$$\frac{d}{dt}\frac{\partial T}{\partial \dot{q}_i} - \frac{\partial T}{\partial q_i} + \frac{\partial V}{\partial q_i} = Q_i \quad (i = 1, \cdots, n) \tag{12}$$

where q_i is the generalized coordinate, T is the kinetic energy, V is the potential energy, and Q_i is the generalized force corresponding to the generalized coordinate q_i.

For a nonlinear spring system having five links, the kinetic energy and potential energy can be obtained by

$$T = \sum_{i=1}^{4} T_i = \sum_{i=1}^{4} \left[\frac{1}{2} m_i |\mathbf{v}_{ci}|^2 + \frac{1}{2} I_i \dot{\theta}_i^2 \right] \tag{13}$$

$$V = \frac{1}{2} k (s_o + y)^2 \tag{14}$$

where v_{ci} is the velocity vector of link i and I_i is the moment of inertia of link i. The generalized forces, which are nonconservative forces, can be expressed as

$$Q = \begin{bmatrix} 0 & 0 & 0 & T_{\text{in}} \end{bmatrix}^T \tag{15}$$

where the angle θ_4 of link 4 has been chosen as the generalized coordinate.

Substitution of Eqs. (13) and (14) into Eq. (12) yields

$$\frac{d}{dt}\left(\sum_{i=1}^{4} \left[m_i |v_{ci}| \frac{\partial |v_{ci}|}{\partial \dot{\theta}_4} + I_i \dot{\theta}_i \frac{\partial \dot{\theta}_i}{\partial \dot{\theta}_4} \right] \right) - \sum_{i=1}^{4} m_i |v_{ci}| \frac{\partial |v_{ci}|}{\partial \theta_4} + k(s_o + y) \frac{\partial y}{\partial \theta_4} = T_{\text{in}} \tag{16}$$

The angular displacement of link 2 is given by

$$\theta_2 = \cos^{-1}\left[\frac{d_o \cot \theta_4 - l_2 \cos \gamma_o}{l_2} \right] \tag{17}$$

and the velocity vector of the mass center of each link is given by

$$\begin{Bmatrix} |\mathbf{v}_{c1}|^2 \\ |\mathbf{v}_{c2}|^2 \\ |\mathbf{v}_{c3}|^2 \\ |\mathbf{v}_{c4}|^2 \end{Bmatrix} = \begin{Bmatrix} l_2^2 \dot{\theta}^2 \sin^2 \theta_2 \\ (l_2^2 - 2 l_2 l_{c2}) \sin^2 \theta_2 \dot{\theta}_2^2 + l_{c2}^2 \dot{\theta}_2^2 \\ l_2^2 \cos^2 \theta_2 \dot{\theta}_2^2 \\ l_4^2 \dot{\theta}_4^2 \end{Bmatrix} \tag{18}$$

where l_{ci} is the distance between the mass center and the joint axis of link i.

By substituting Eqs. (17) and (18) into Eq. (16), the dynamic differential equation of motion of the nonlinear spring system is obtained in the form of

$$\ddot{\theta}_4 = f(\theta_4, \dot{\theta}_4) \tag{19}$$

Since Eq. (19) is a second-order nonlinear ordinary differential equation representing the angular displacement θ_4 and the angular velocity $\dot{\theta}_4$ of the input link, it is numerically solved for the dynamic motion analysis by using the fourth-order and fifth-order Runge–Kutta ordinary differential equation solver offered in the MATLAB/SIMULINK package.

As the input torque $T_{\text{in}}(t)$ acting on the input link (link 4) increases linearly, θ_4 is changed as shown in Fig. 7(*b*). In this analysis, each parameter is set to the same value as in the preceding example so I_{G2}=0.55 kg mm^2, I_{G4}=0.06 kg mm^2, l_2=26 mm, m_1=0.015 kg, m_2=0.01 kg, m_3=0.015 kg, and m_4=0.02 kg. The threshold torque is 8.0 N m as calculated using Eq. (9).

When the input torque increases from 0 N m to 8.0 N m, which is below the threshold torque, the output slider (link 3) and the input link (link 4) do not move, as shown in Fig. 7(*b*). As the input torque $T_{\text{in}}(t)$ increases above the threshold torque, the static equilibrium cannot be maintained and the output slider starts moving. Once the output slider moves and the input link rotates, the equivalent stiffness of this mechanism (k_{eq} in Fig. 5(*b*)) rapidly decreases and, thus, the output slider moves rapidly upside.

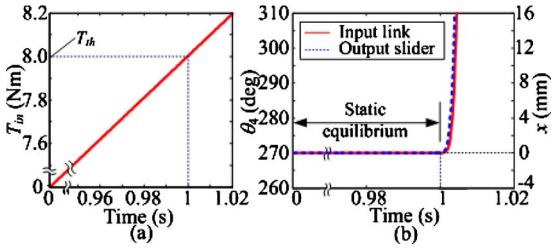

Fig. 7 Dynamic analysis of the nonlinear spring system: (*a*) input torque versus time and (*b*) angular displacement of input link and displacement of output slider versus time

The nonlinear motion of this mechanism can be explained as follows. When the input torque T_{in} is 8.0 N m (point a), which is the same as the spring torque T_s (point a′) in Fig. 8, this mechanism can maintain static equilibrium. As T_{in} increases to 8.07 N m (point b) in Fig. 8, T_s decreases to 4.8 N m (point b′). Although F_s increases during the process a′→b′, as discussed in Sec. 2.1, T_s decreases because of the decrease in the transmission angle of the double-slider mechanism, as shown in Fig. 5(*a*). Therefore, this difference between T_{in} and T_s initiates the nonlinear motion of this mechanism. For example, when T_{in} becomes 8.1 N m (point c), which is only 0.1 N m larger than T_{th}, θ_4 reaches 298 deg and T_s drops abruptly to 2.8 N m (point c′).

In summary, the stiffness of the proposed nonlinear spring system remains very high, such as a hard spring while the input torque is below the threshold torque. However, as the input torque becomes larger than the threshold, the stiffness abruptly drops, thus causing this nonlinear spring to behave as a soft spring.

3 Safe Joint Mechanism Model

3.1 Prototype Modeling. The nonlinear spring system introduced conceptually in the previous section is now realized into a SJM-II, which can lead to a novel design of a safe robot arm. The SJM-II consists of a double-slider mechanism, a linear spring, and a force transmission plate, as shown in Fig. 9.

As shown in Fig. 9, the input slider (link 1 in Fig. 4) and the output slider (link 3 in Fig. 4) are replaced by roller 1 and roller 2, which slide along slot 1 and slot 2 of the fixed plate, respectively. The fixed plate is connected with a nonback-drivable joint actuator. The input link (link 4 in Fig. 4) is replaced by a force transmission bar. Since the force transmission bar is fixed to the robot link, the external force acting on the distal end of the robot link generates the input torque, which causes the force transmission bar of the SJM-II to exert the force on roller 1. Notice that the input torque shown in Fig. 9(*b*) is usually generated by the exter-

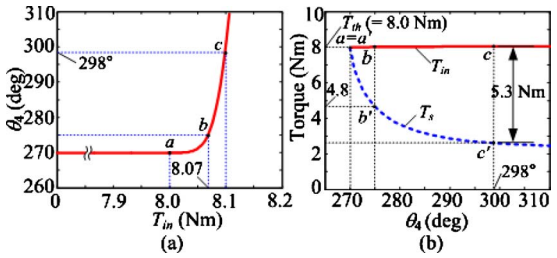

Fig. 8 Dynamic analysis of the nonlinear spring system: (*a*) angular displacement versus input torque and (*b*) comparison between input torque and torque by spring force

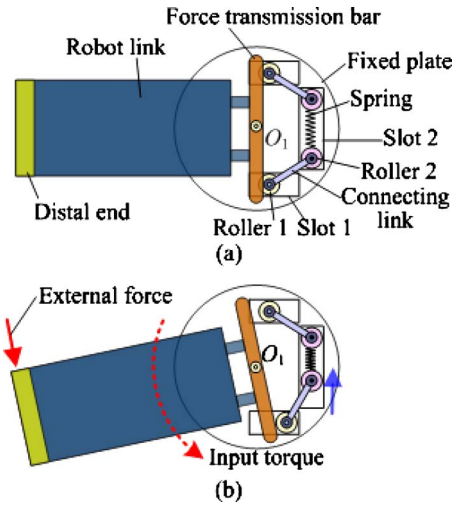

Fig. 9 Operation of SJM-II: (*a*) before collision and (*b*) after collision

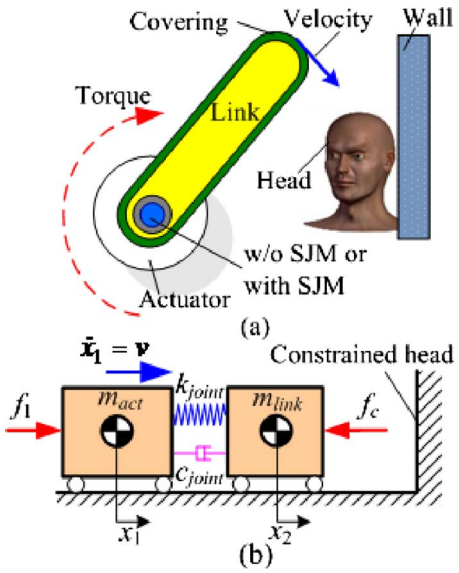

Fig. 10 Collision model between human head and robot arm: (*a*) concept collision model (*b*) simplified collision model

nal force at the distal end. Two double-slider mechanisms are arranged symmetrically so that they can absorb the external force applied in both directions.

Since the point of application of the external force is always changing, it is convenient to describe the operation of the SJM-II in terms of the input torque shown in Fig. 9(*b*). If the input torque exceeds a threshold torque, as shown in Fig. 9(*b*), the input link is rotated around O_1. Then, roller 2 connected to the connecting link is forced to move on slot 2 in the direction of compressing the spring. This movement of roller 2 reduces the transmission angle so maintaining static balance requires a much greater resisting force for the same external force at the distal end of the robot arm. However, the increased spring force due to its compression is not large enough to sustain this balance as introduced in Sec. 2.2. This unbalance causes roller 2 to rapidly slide in the direction of spring compression. As a result, the force transmission bar rotates and the robot arm also turns, thus, absorbing the external force. However, if the input torque is less than the threshold torque, the distal end does not rotate at all, and the double-slider mechanism maintains static equilibrium and, thus, the SJM-II can provide high stiffness for the joint of the robot arm.

3.2 Collision Analysis. Some studies have been conducted on collision safety between a human and a robot without clamping the head [10,13,14]. In this study, it was assumed that a human head was constrained at the wall, which corresponds to much more severe condition than the case in which the head can move freely after head impact. Furthermore, the initial conditions and parameters of the collision model were realistically modified. As shown in Fig. 10, the robot arm with and without the SJM was modeled as a 2-DOF mass-spring-damper system. In this modeling, the quantities (e.g., moment of inertia and torque) in joint space were converted into those (e.g., reflected inertia and force) in Cartesian space using the Jacobian relation. The input torque applied to the robot joint makes the robot link follow the desired position and the end-point of the robot link with a urethane covering collides with a nasal bone of the constrained human head.

The equation of motion is given by

$$M\ddot{X} + C\dot{X} + KX = F \tag{20}$$

where M, C, K, X, and F are the mass matrix, damping matrix, stiffness matrix, displacement vector, and force vector, respectively. The mass, stiffness, and damping matrices are given by

$$M = \begin{bmatrix} m_{\text{act}} & 0 \\ 0 & m_{\text{link}} \end{bmatrix} \tag{21a}$$

$$K = \begin{bmatrix} k_{\text{joint}} & -k_{\text{joint}} \\ -k_{\text{joint}} & k_{\text{joint}} \end{bmatrix} \tag{21b}$$

$$C = \begin{bmatrix} c_{\text{joint}} & -c_{\text{joint}} \\ -c_{\text{joint}} & c_{\text{joint}} \end{bmatrix} \tag{21c}$$

where m_{act} and m_{link} are the mass of the joint actuator and robot link, respectively, and k_{joint} is the joint stiffness, and c_{joint} is the joint damping.

The displacement and force vectors are given by

$$X = \begin{bmatrix} x_1 & x_2 \end{bmatrix}^T, \quad F = \begin{bmatrix} f_1 & -f_c \end{bmatrix}^T \tag{22}$$

where x_1 and x_2 are the displacements of the actuator and the robot link, respectively, and f_1 is the input force, which corresponds to the joint torque of the robot, and f_c is the contact force between the head and the robot arm. The input force can be obtained using $f_1 = k_p(x_d - x_1) - k_v\dot{x}_1$, where x_d is the desired position and k_p and k_v are the proportional-derivative (PD) gains for position control of the robot arm.

In this study, we adopted the Hunt and Crossley's approach, which represents the contact force between the human head and the robot arm by the Hertz force law with a nonlinear viscous-elastic element [15]. The contact force with hysteresis damping for impact in multibody systems can be described by

$$f_c = k\delta^n\left(1 + \frac{3(1-c_e^2)}{4}\frac{\dot{\delta}}{\dot{\delta}_0}\right) \tag{23}$$

where k is the generalized stiffness constant, c_e is the coefficient of restitution, and δ, $\dot{\delta}$, and $\dot{\delta}_0$ are the relative penetration depth ($=x_2$), the relative normal impact velocity, and the initial impact velocity, respectively. The constants k and c_e and the exponent n depend on the material properties of contacting surfaces.

The joint stiffness of a robot arm without the SJM is the same with that of a speed reducer. For the robot arm with the SJM, the joint stiffness is described by

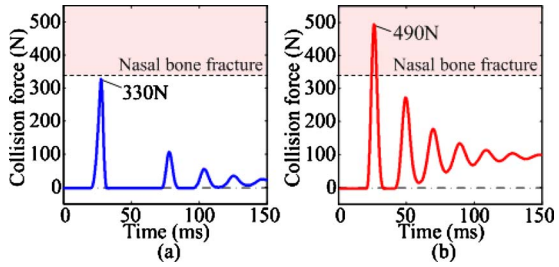

Fig. 11 Analytical results showing impact force versus time during collision with robot arm: (*a*) with SJM-II and (*b*) without SJM-II

$$k_{\text{joint}} = \begin{cases} k_{\text{SJM}}, & x_1 > x_2 \\ k_{\text{reducer}}, & x_1 \le x_2 \end{cases} \tag{24}$$

where k_{reducer} is the stiffness of the speed reducer and k_{SJM} is the stiffness of the SJM obtained from Eq. (11).

Since Eq. (20) is a coupled second-order nonlinear differential equation in the displacement vector X, it must be solved numerically for this analysis. From Eq. (20), the differential equation of motion for the collision model is expressed as

$$\ddot{X} = M^{-1}(F - C\dot{X} - KX) \tag{25}$$

The numerical analysis was conducted using the fourth-order and the fifth-order Runge–Kutta ordinary differential equation solver offered in the MATLAB/SIMULINK package. In this analysis, $m_{\text{act}}=6$ kg, $m_{\text{link}}=1$ kg, $k_{\text{reducer}}=256$ kN/m, $c_{\text{reducer}}=10$ Ns/m, $x_d=0.5$ m, $k_p=250$, $k_v=70$, $k=6.1\times10^6$ N/m$^{1.5}$, and $n=3.0$ and the initial conditions are $X=[-1\ \ -1]^T$ and $\dot{X}=[0\ \ 0]^T$; the collision speed between the human head and the robot link was set to 1.5 m/s.

For the robot arm without the SJM, as shown in Fig. 11(*b*), the collision force reached a peak value of 490 N and the collision force after collision was about 100 N. However, for the robot arm equipped with the SJM, the peak force decreased to 330 N and the collision force after the collision also were much lower than that without the SJM, as shown in Fig. 11(*a*). It was verified that the robot arm with the SJM provides much higher safety for physical human-robot contact than that without the SJM because the amount of the impulse with the SJM is much smaller than without the SJM.

4 Experiments for Safe Joint Mechanism

4.1 Prototype of SJM. The prototypes of the SJM-II shown in Fig. 12 were constructed to conduct various performance experiments. The sizes of the SJM-IIs is $\phi\,65\times25$ mm^2, its weight is 120 g, and its threshold torques is 8.2 Nm. Most components are made of duralumin, which can endure the shock exerted on the SJM. The SJM-II can be easily installed at the joint of the robot arm.

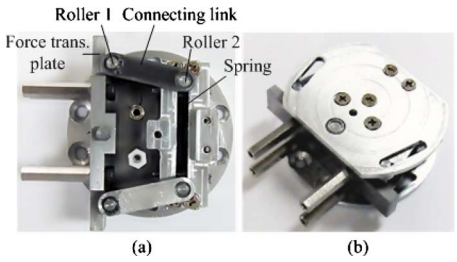

Fig. 12 Prototype of the SJM-II

Table 1 Injury tolerance of body parts

Cranial bone [21]	Fracture tolerance (kN)
Frontal	4.0
Temporal	3.12
Occipital	6.41
Facial bone [22]	**Fracture tolerance (kN)**
Mandible (center)	1.89
Mandible (lateral)	0.82
Maxilla	0.62
Zygomatic	0.85
Nasal	0.34
Other body parts	**Injury tolerance**
Chest compression [23]	22 mm
Chest viscous criterion [24]	0.5 m/s
Pain tolerance [25]	50 N

4.2 Safety Criterion. Although some studies of collision safety between a human and a robot have been conducted [16,17], safety criteria for physical human-robot interaction do not exist except in ISO-10218 [18], which defines collaborative operation requirements for industrial robots. Since these requirements strongly restrict the performance of a robot arm, they are not suitable to use as the safety criteria for physical human-robot interaction. Therefore, to evaluate the potential injury caused by collision, the head injury criterion and the abbreviated injury scale are typically used [19]. Recently, it was claimed that these criteria are not an appropriate measure of injury severity in robotics because no robot exceeds their critical safety thresholds. This is due to the much lower collision speed between a robot and a human than would be the case for humans in an automobile crash [20]. Therefore, the fracture force of the facial and cranial bones and the compression and viscous criterion of the chest were suggested for defining more relevant injury mechanisms as shown in Table 1.

Since most service robots, unlike industrial robots, have low inertia and low speed, a lower level criterion than the fracture force limit is needed to estimate the danger of collision. Therefore, in this research, the injury tolerance of facial bone and the pain tolerance were used as the safety criteria.

4.3 Experimental Results. Figure 13 shows an experimental setup in which the SJM-II ($T_{\text{th}}=8.2$ Nm) was installed at joint 2 of a 2-DOF robot arm. The motor torques applied to joint 1 and joint 2 were transmitted to the robot link 1 and robot link 2, respectively. The lengths of robot link 1 and robot link 2 were 0.4 m and 0.34 m, respectively.

A force sensor was installed at an end-point of the robot arm to measure the collision force between the impactor and the dummy head. The angular displacement of the SJM-II can be obtained from the angle difference between the encoder attached to a motor and the extra encoder, which can measure the angular displacement of robot link 2. For example, when the SJM rotates 20 deg after it absorbs the collision force, the angle difference between those encoders becomes 20 deg. The dummy head, which weight (4.5 kg) and size (ϕ 20 cm) are similar with those of the human head was constructed. This dummy was made with the polyoxymethylene, which can endure the shock exerted on the collision.

In the experiment for static collision, the spring constant was 5.6 kN/m, its compression was 16 mm, and the transmission angle was 165 deg at the zero configuration. The impactor of the robot arm was initially placed to barely touch a fixed dummy head and the joint torque provided by the motor was slowly increased. The static collision force between the robot and the dummy was

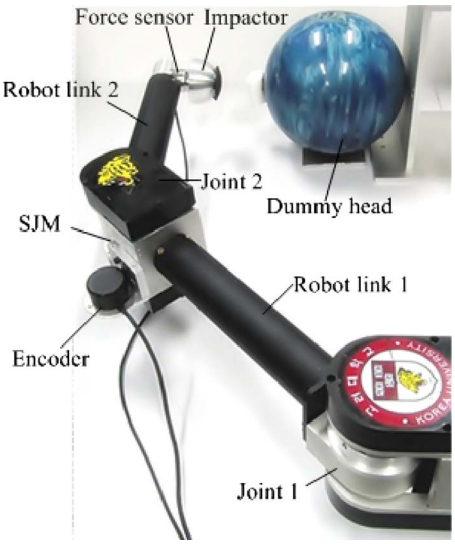

Fig. 13 Experimental setup for robot arm with SJM-II

measured by a force sensor. Experiments were conducted for the robotic arms with and without the SJM.

The robot arm without the SJM-II delivered a contact force that increased up to 60 N at the wall due to high stiffness of the speed reducer. However, a contact force of up to 24 N was transmitted to the wall for the robot arm with SJM-II, as shown in Fig. 14. Although the motor continually rotated after collision, the contact force decreased to 10 N.

A contact force above pain tolerance does not occur because the excessive force is absorbed by the SJM. As shown in Fig. 14(*b*), virtually no displacement of the robot arm occurred when the external torque due to the contact force was below the threshold force of 24 N. Therefore, the robot arm with the SJM can accurately handle a payload of up to approximately 2.0 kg as though it had a speed reducer with a high gear ratio. As the input torque increased above the threshold torque, the stiffness of the SJM quickly diminished thus maintaining the robot arm in the safe region. In summary, the SJM provides high positioning accuracy of the robot arm in the working region and guarantees safe human-robot contact by absorbing contact force above 50 N in the unsafe region.

Next, some dynamic collision experiments were conducted for the robot arm equipped with the SJM-II. The experimental conditions, including the spring constant, the compression length of the spring, and the transmission angle at the zero configuration, were set to the same values as those of the static collision experiments. For dynamic collision, a robot link rotating at an angular velocity of 118 deg/s, which corresponds to an end-point velocity of 1.5

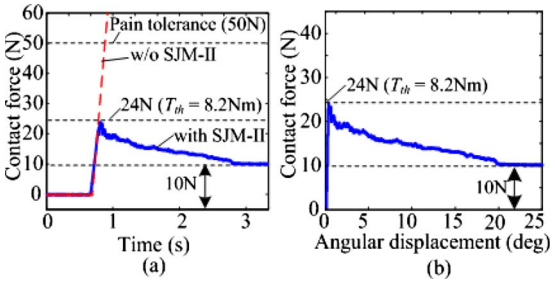

Fig. 14 Experimental results for static collision for robot arm: (*a*) collision force versus time with and without SJM-II and (*b*) collision force versus angular displacement of SJM-II

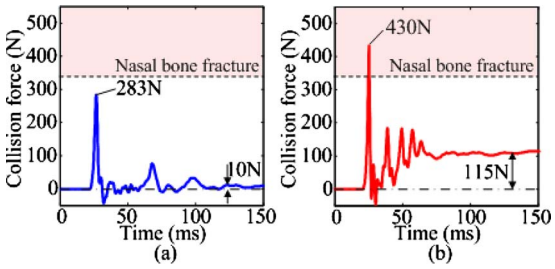

Fig. 15 Experimental results on dynamic collision: (*a*) with SJM-II and (*b*) without SJM-II

m/s, was forced to collide with a dummy head that has a nose. The collision force between the dummy head and the robot link was measured by a force sensor mounted at the impactor.

The experimental results are shown in Fig. 15. At the instant the robot arm with the SJM-II contacted the nasal bone of the constrained dummy head, collision forces reached peak values of 283 N but immediately after collision, collision forces delivered to the head dropped rapidly below 10 N because of the operation of the SJM. Therefore, safe human-robot contact can be achieved even for this harsh dynamic collision.

Figure 15(*b*) shows experimental results for a dynamic collision of the robot arm without the SJM-II. The peak value of the collision force to the nose were almost 1.5 times that of the robot arm with the SJM-II, which is above the fracture tolerance of the nasal bone, and the collision force after collision was more than the human pain tolerance of 50 N. Therefore, the robot arm with the SJM provides much higher safety for human-robot contact than the arm without the SJM-II. Furthermore, comparison of Fig. 15 with Fig. 11 shows that the experimental results are in good agreement with analysis results mentioned in Sec. 3.2 in terms of the peak value of the collision force, the shape of the collision force curve, and the residual collision force.

To compare the SJM-II with a torque limiter, some experiments were conducted for the robotic arms equipped with the SJM and a torque limiter. The torque limiter of R+W (SK2 model) was used in this experiment and its limit torque was set to 8 Nm. As shown in Fig. 16, the robot arm was forced to rotate to 35 deg and rotate back to its initial position. When the robot arm rotated at 15 deg, its end-point touched a constrained dummy head. To measure the collision force and the angular displacement of the torque limiter, a force sensor and an extra encoder were used in the same manner as the previous experiments.

As shown in Fig. 17(*a*), for the collision with the dummy, the robot arm with the torque limiter delivered a contact force whose peak was 29 N to the head, which is similar to the SJM-II. However, after the collision force was removed, the robot link with the SJM-II could return to the position just before the collision, whereas that with the torque limiter could not, as shown in Fig. 17(*b*) in which its angular displacement was maintained a phase

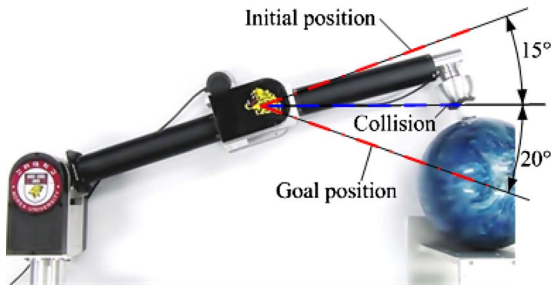

Fig. 16 Experimental setup for comparison between SJM-II and torque limiter

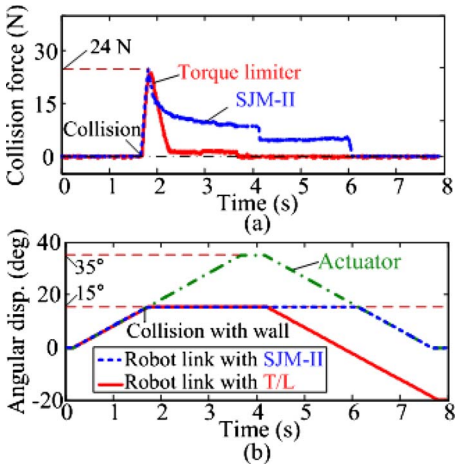

Fig. 17 Experimental results on static collision for robot arm with SJM-II and torque limiter: (*a*) collision force and (*b*) angular displacement of robot link

difference of 20 deg. This is the main reason the torque limiter cannot be used for a robot arm as a safety mechanism.

5 Conclusions

In this research, a safe joint mechanism-II was proposed for collision safety. A robot arm equipped with the SJM-II can maintain very high stiffness up to a preset threshold torque but provides a very low stiffness above the threshold. From the analysis and experiments, the following conclusions are drawn.

(1) Stiffness of the robot manipulator abruptly drops if the input torque to the SJM-II exceeds the predetermined threshold torque. Therefore, collision safety can be achieved even for a high-speed dynamic collision.
(2) High stiffness of the robot arm can be maintained for input torque that is lower than the threshold torque. Therefore, positioning accuracy can be achieved in normal operation.
(3) The proposed SJM-II is based on passive compliance so it shows faster response and higher reliability than the designs based on active compliance with sensors and actuators.
(4) Since the SJM-II is simple enough to be installed between an actuator and a robot link, it can be applied to any type of robot arm without much modification of the robot design.

Currently, simpler and more lightweight safe joint mechanisms are under development so that several SJM-IIs may be used simultaneously in the robot arm without much increase in cost and weight.

Acknowledgment

This work was supported by the Center for Autonomous Intelligent Manipulation under the Human Resources Development Program for Convergence Robot Specialists, by the Development of Manipulation Technology for Human-Robot Cooperation, and by the Korea University research fund.

References

[1] Albu-Schaeffer, A., Eiberger, O., Grebenstein, M., Haddadin, S., Ott, Ch., Wimboeck, T., Wolf, S., and Hirzinger, G., 2008, "Soft Robotics: From Torque Feedback Controlled Lightweight Robots to Intrinsically Compliant Systems," IEEE Robot. Autom. Mag., **15**(3), pp. 20–30.
[2] Moosavian, S. A., and Papadopoulos, E., 2010, "Cooperative Object Manipulation With Contact Impact Using Multiple Impedance Control," International Journal of Control, Automation, and Systems, **8**(2), pp. 314–327.
[3] Yoo, S.-J., Park, J.-B., and Choi, Y.-H., 2008, "Output Feedback Dynamic Surface Control of Flexible-Joint Robots," International Journal of Control, Automation, and Systems, **6**(2), pp. 223–233.
[4] Shin, D., Sardellitti, I., and Khatib, O., 2008, "A Hybrid Actuation Approach for Human-Friendly Robot Design," Proceedings of the IEEE International Conference on Robotics and Automation, pp. 1747–1752.
[5] Filippini, R., Sen, S., and Bicchi, A., 2008, "Toward Soft Robots You Can Depend On," IEEE Robot. Autom. Mag., **15**(3), pp. 31–41.
[6] Damme, M. V., Vanderborght, B., Verrelst, B., Ham, R. V., Daerden, F., and Lefeber, D., 2009, "Proxy-Based Sliding Mode Control of a Planar Pneumatic Manipulator," Int. J. Robot. Res., **28**, pp. 266–284.
[7] Morita, T., and Sugano, S., 1995, "Development of One DOF Robot Arm Equipped With Mechanical Impedance Adjuster," Proceedings of the IEEE/RSJ International Conference on Intelligent Robots and System, pp. 407–412.
[8] Wolf, S., and Hirzinger, G., 2008, "A New Variable Stiffness Design: Matching Requirements of the Next Robot Generation," Proceedings of the IEEE International Conference on Robotics and Automation, pp. 1741–1746.
[9] Knox, T. B., and Schmiedeler, J. P., 2009, "A Unidirectional Series-Elastic Actuator Design Using a Spiral Torsion Spring," ASME J. Mech. Des., **131**(12), p. 125001.
[10] Park, J.-J., Kim, B.-S., Song, J.-B., and Kim, H.-S., 2008, "Safe Link Mechanism Based on Nonlinear Stiffness for Collision Safety," Mech. Mach. Theory, **43**, pp. 1332–1348.
[11] Park, J.-J., Lee, Y.-J., Song, J.-B., and Kim, H.-S., 2008, "Safe Joint Mechanism Based on Nonlinear Stiffness for Safe Human-Robot Collision," Proceedings of the IEEE International Conference on Robotics and Automation, pp. 2177–2182.
[12] Park, J.-J., Kim, H.-S., and Song, J.-B., 2009, "Safe Robot Arm With Safe Joint Mechanism Using Nonlinear Spring System for Collision Safety," Proceedings of the IEEE International Conference on Robotics and Automation, pp. 3371–3376.
[13] Bicchi, A., and Tonietti, G., 2004, "Fast and Soft Arm Tactics: Dealing With the Safety-Performance Tradeoff in Robot Arms Design and Control," IEEE Robot. Autom. Mag., **11**(2), pp. 22–33.
[14] Morita, T., Iwata, H., and Sugano, S., 2000, "Human-Symbiotic Robot Design Based on Division and Unification of Functional Requirements," Proceedings of the IEEE International Conference on Robotics and Automation, pp. 2229–2234.
[15] Lankarani, H. M., and Nikravesh, P. E., 1990, "A Contact Force Model With Hysteresis Damping for Impact Analysis of Multibody Systems," ASME J. Mech. Des., **112**, pp. 369–376.
[16] Oberer, S., and Schraft, R. D., 2007, "Robot-Dummy Crash Tests for Robot Safety Assessment," Proceedings of the IEEE International Conference on Robotics and Automation, pp. 2934–2939.
[17] Wassink, M., and Stramigioli, S., 2007, "Towards a Novel Safety Norm for Domestic Robotics," Proceedings of the IEEE/RSJ International Conference on Intelligent Robots and Systems, pp. 3354–3359.
[18] ISO10218, 2006, Robots for Industrial Environments—Safety Requirements—Part 1: Robot.
[19] Versace, J., 1971, "A Review of the Severity Index," Proceedings of the 15th Stapp Car Crash Conference, pp. 771–796.
[20] Haddadin, S., Albu-Schaffer, A., and Hirzinger, G., 2008, "The Role of the Robot Mass and Velocity in Physical Human-Robot Interaction – Part I: Non-Constrained Blunt Impacts," Proceedings of the IEEE International Conference on Robotics and Automation, pp. 1331–1338.
[21] 1980, "Human Tolerance to Impact Conditions as Related to Motor Vehicle Design," SAE Paper No. J885 APR 80.
[22] Nahum, A. M., 1972, "Impact Studies of Facial Bones and Skull.," Proceedings of 16th Stapp Car Crash Conference, pp. 8–10, SAE Technical Paper No. 720965.
[23] Lau, I., and Viano, D., 1983, "Role of Impact Velocity and Chest Compression in Thoracic Injury," Aviat Space Environ. Med., **54**(1), pp. 16–21.
[24] Lau, I., and Viano, D., 1986, "The Viscous Criterion-Bases and Applications of an Injury Severity Index for Soft Tissues," Proceedings of 30th Stapp Car Crash Conference, SAE Technical Paper No. 861882.
[25] Yamada, Y., Hirasawa, Y., Huang, S. Y., and Umetani, Y., 1996, "Fail-Safe Human/Robot Contact in the Safety Space," IEEE International Workshop on Robot and Human Communication, pp. 59–64.